

# Assimilation of the AMSU-A radiances using the CESM (v2.1.0) and the DART (v9.11.13)/RTTOV (v12.3)

Young-Chan Noh<sup>1</sup>, Yonghan Choi<sup>1</sup>, Hyo-Jong Song<sup>2</sup>, Kevin Raeder<sup>3</sup>, Joo-Hong Kim<sup>1</sup>, and Youngchae Kwon<sup>2</sup>

<sup>1</sup> Korea Polar Research Institute, Incheon, 21990, South Korea

<sup>2</sup> Department of Environmental Engineering and Energy, Myongji University, Seoul, 17058, South Korea

<sup>3</sup> National Center for Atmospheric Research, CISL/DAReS, Boulder, CO, 80305, USA

*Correspondence to:* Yonghan Choi (yhdchoi@kopri.re.kr)

**Abstract.** To improve the initial condition (“analysis”) for numerical weather prediction, we attempt to assimilate observations from the Advanced Microwave Sounding Unit-A (AMSU-A) on board the low-earth-orbiting satellites. The data assimilation system, used in this study, consists of the Data Assimilation Research Testbed (DART) and the Community Earth System Model as the global forecast model. Based on the ensemble Kalman filter scheme, DART supports the radiative transfer model that is used to simulate the satellite radiances from the model state. To make the AMSU-A data available to be assimilated in DART, preprocessing modules are developed, which consist of quality control, spatial thinning, and bias correction processes. In the quality control, two sub-processes are included: outlier test and channel selection depending on the cloud condition and surface type. The bias correction process is divided into scan-bias correction and air-mass-bias correction. As input data used in DART, the observation errors are also estimated for the AMSU-A channels. In the trial experiments, a positive analysis impact is obtained by assimilating the AMSU-A observations on top of the DART data assimilation system that already makes use of the conventional measurements. In particular, the analysis errors are significantly reduced in the whole troposphere and lower stratosphere over the Northern Hemisphere. Overall, this study demonstrates a positive impact on the analysis when the AMSU-A observations are assimilated in the DART assimilation system.

## 1 Introduction

Data assimilation is a numerical procedure for making the initial condition (“analysis”) that is used as the starting point for a numerical weather prediction (NWP). In the data assimilation process, various observation data are combined with the short-term forecast (“background”) derived from the NWP model, based on the error characteristics of the observations and model forecast (Kalnay, 2003). With the huge amount of satellite observations and advances in model configurations (e.g., horizontal/vertical resolution and dynamic core) and data assimilation, the quality of the initial condition significantly increases, which enhances the forecast skill. In particular, the initial condition has dramatically improved since the satellite observations started to be assimilated (Migliorini et al., 2008; Eyre et al., 2020; Eyre et al., 2022). It is because the satellites cover the regions where the conventional observations are sparse or absent. Among many types of satellite observations being assimilated, a significant forecast benefit mainly comes from the observations of the hyperspectral infrared and microwave sounders that provide unique information on the vertical structure of key atmospheric parameters (e.g., temperature and moisture) (Joo et al., 2013; Eresmaa et al., 2017; Menzel et al., 2018). For this reason, satellite observations are actively being assimilated into the data assimilation system in many operational NWP centers.

To advance the research related to data assimilation, a well-organized data assimilation system is essential, which consists of the forecast model, a data assimilation scheme, and flexible interfaces to use various types of observations. Operational NWP centers have well-constructed assimilation systems to use diverse types of available observations with up-to-date data assimilation schemes. However, as most operational global NWP systems require huge computation resources, it is practically impossible for researchers to recreate those systems outside of the NWP centers. Thus, a user-friendly global data

40 assimilation system is needed for small numerical modeling communities to attempt challenging studies related to advancing  
41 the data assimilation quality.

42 The National Center for Atmospheric Research (NCAR) has developed an open-source data assimilation tool that is  
43 named the Data Assimilation Research Testbed (DART) for data assimilation research, development, and education (Anderson  
44 et al., 2009). DART has interfaces to diverse Earth system components (e.g., atmosphere, ocean, and cryosphere) developed  
45 by many modeling centers. For instance, the Community Atmospheric Model (CAM), the atmospheric component of the  
46 Community Earth System Model (CESM) developed by NCAR, can be used to provide the short-range forecast that is the  
47 background field in DART. DART is based on the ensemble data assimilation method instead of the variational method, which  
48 requires complicated software specific to a particular numerical prediction model (Anderson et al., 2009; Raeder et al., 2012).  
49 In addition, well-defined modules are included to make various types of observations available in the DART data assimilation  
50 process. Thus, DART can assimilate many observation types (e.g., conventional and satellite-based wind). Liu et al. (2012)  
51 investigated the impact of the Global Positioning System (GPS) Radio Occultation (RO) observations on the forecast of  
52 Hurricane Ernesto (2006) using the DART assimilation system. Coniglio et al. (2019) showed that additional forecast benefit  
53 is made by assimilating the measurements of ground-based wind profilers. In addition, a decade-long reanalysis was created  
54 with 80 ensemble members derived from DART, using ground-based data, satellite-based winds, GPS-RO observations, and  
55 temperature soundings retrieved from the Atmospheric Infrared Sounder (AIRS) observation (Raeder et al., 2021).

56 However, there are few studies of assimilating satellite-measured radiances in the DART data assimilation system,  
57 because the previous version of DART did not have the essential components, e.g., the radiative transfer model (RTM), needed  
58 to simulate the satellite radiances from the model state. Fortunately, in the recent version of DART (version 9.11.13), the RTM  
59 is included. The Radiative Transfer for TIROS Operational Vertical Sounder (RTTOV) version 12.3 is supported to map the  
60 model space into observation space in the data assimilation scheme (Saunders et al., 2018). In Zhou et al. (2022), the visible  
61 imagery of the Chinese geosynchronous-orbiting (GEO) satellite was assimilated in DART, but using the Observing System  
62 Simulation Experiment (OSSE) framework in which the visible imagery was simulated and then assimilated. Considering that,  
63 it is interesting to assimilate the satellite-observed radiances using the DART data assimilation system to know how the analysis  
64 derived from DART is affected by real satellite observations.

65 Considering the fact that the analysis/forecast impact derived from the satellite radiances mainly comes from  
66 observations of hyperspectral infrared and microwave sounders (English et al., 2013; Joo et al., 2013; Kim and Kim, 2019), it  
67 is reasonable to assimilate the observations of both sounders first. Unfortunately, the use of hyperspectral infrared sounder  
68 observations was not supported in the recent version of DART. For this reason, we attempt to assimilate the radiances of the  
69 Advanced Microwave Sounding Unit-A (AMSU-A) temperature sounder within the DART data assimilation system coupled  
70 with the NCAR CESM. AMSU-A instruments are currently operating on board many low-earth-orbiting (LEO) satellite  
71 platforms, and thus a large amount of AMSU-A observation data is available for assimilation. In addition, as the microwave  
72 sounder observations are less sensitive to clouds than the infrared sounder observations, the data availability of AMSU-A is  
73 better than that of the infrared sounder. AMSU-A observations are actively used to improve global/regional forecasts as well  
74 as severe weather forecasts such as tropical cyclones (Zhang et al., 2013; Zhu et al., 2016; Migliorini and Candy, 2019; Duncan  
75 et al., 2022). As the preprocessing modules (e.g., quality control, cloud detection, and spatial thinning) for AMSU-A  
76 observations are not provided in the DART package, they are developed in this study. In addition, the diagonal observation  
77 error covariance matrix is estimated using the method suggested by Desroziers et al. (2005), and a bias correction scheme is  
78 also developed based on the methods suggested by Harris and Kelly (2001). In this study, we attempt to assimilate the AMSU-  
79 A radiances in clear-sky conditions. In many operational NWP centers, the AMSU-A radiances have been assimilated in all-  
80 sky conditions (i.e., clear-sky and cloudy-sky) (Zhu et al., 2016; Migliorini and Candy, 2019; Duncan et al., 2022). However,  
81 as the current version of DART is not ready to assimilate the AMSU-A radiances in cloudy-sky conditions, only the clear-sky  
82 assimilation of AMSU-A radiances is considered. To assess the impact of assimilating AMSU-A observations on the analysis

83 derived from DART, the assimilation experiments are conducted using the DART assimilation system coupled with the CESM  
84 as the forecast model system.

85 This paper is organized as follows. Section 2 provides the background information on the DART data assimilation  
86 system and CESM. Observation data assimilated in DART are described in section 3. The developed preprocessing steps and  
87 the estimated observation errors are presented in sections 4 and 5, respectively. The setup of the assimilation experiments is  
88 explained in section 6. The results of the first-guess/analysis departure analysis and the analysis impact are explored in section  
89 7, followed by a summary in section 8.

## 90 **2 DART-CESM data assimilation system**

### 91 **2.1 Data Assimilation Research Testbed (DART)**

92 DART is an open-source assimilation package that has been developed by NCAR since 2002 for data assimilation  
93 development, research, and education. DART can be coupled with full-complexity Earth system components due to the flexible  
94 interfaces provided. In addition, the DART package provides the modules to convert observation data from a variety of native  
95 formats, e.g., the Binary Universal Form for the Representation of meteorological data (BUFR) format and the Hierarchical  
96 Data Format (HDF), into the input format specified for the DART system (Anderson et al., 2009; Raeder et al., 2012). The  
97 recent version of DART (version 9.11.13) is capable of using the RTTOV, a fast RTM, for assimilating visible, infrared, and  
98 microwave satellite observations. Provided in RTTOV, many satellite instruments on board the GEO and LEO satellites are  
99 also supported in the DART assimilation package, but the hyperspectral infrared sounders, e.g., the Cross-track Infrared  
100 Sounder (CrIS) and the Infrared Atmospheric Sounding Interferometer (IASI), are excluded (Hoar et al., 2020). The main data  
101 assimilation technique provided by DART is the ensemble Kalman filter (EnKF) in which the forecast error covariance is  
102 estimated using short-range ensemble forecasts. The derived forecast error covariance is fully multivariate and depends on the  
103 synoptic situation.

### 104 **2.2 Community Earth System Model (CESM)**

105 CESM version 2 (CESM v2.1.0) is used as the model component of the ensemble data assimilation system. CESM2  
106 is the latest generation of coupled climate/earth modeling system developed by NCAR, consisting of the atmosphere, land  
107 surface, ocean, sea-ice, land-ice, river, and wave models. These component models can be coupled to exchange states and  
108 fluxes (Hurrell et al., 2013; Kay et al., 2015). In this study, atmosphere and land component models are actively coupled, but  
109 the ocean component (sea surface temperature) and sea ice coverage are specified by data read from files. As the atmosphere  
110 model of CESM2, CAM version 6 (CAM6) is an atmospheric general circulation model (AGCM) with the Finite Volume (FV)  
111 dynamical core (Danabasoglu et al., 2020). CAM6 provides the short-term forecast (6-h forecast) of the atmospheric state,  
112 which is used as the background state in the DART assimilation scheme. The land model is the Community Land Model  
113 version 5 (CLM5). The atmospheric variables are directly updated by the information derived from the observations ingested  
114 in the DART assimilation process, while the land state is affected interactively by the updated atmosphere state because the  
115 two component models are coupled. The two active models (CAM6 and CLM5) are run with a nominal  $1^\circ$  ( $1.25^\circ$  in longitude  
116 and  $0.95^\circ$  in latitude) horizontal resolution. CAM6 has 32 vertical levels from the surface level to the top at 3.6 hPa (about 40  
117 km).

## 118 **3 Observations**

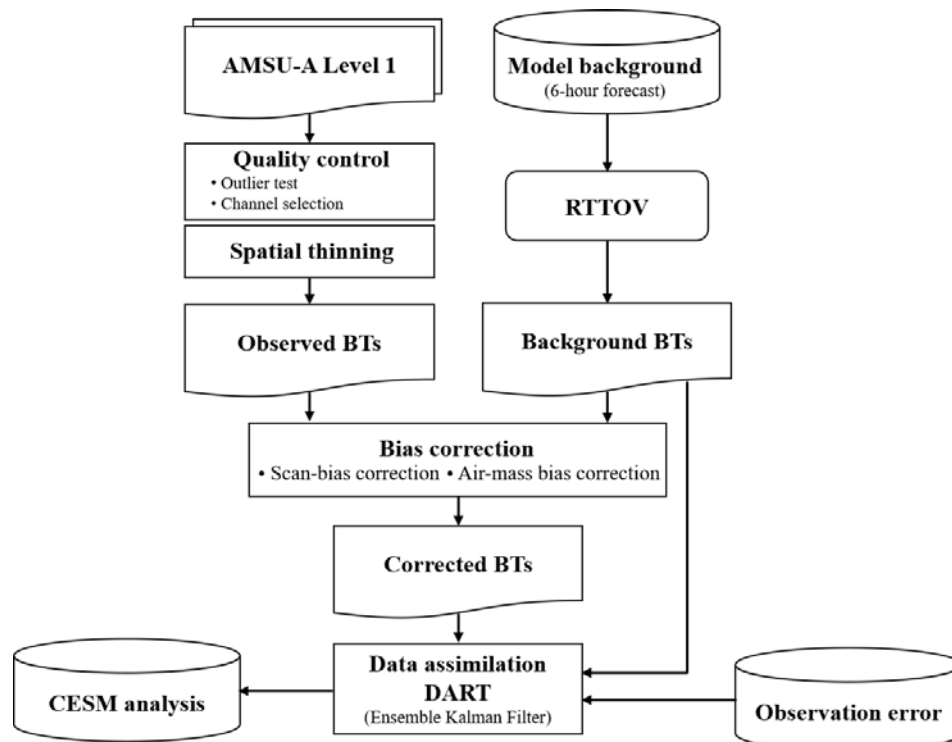
### 119 **3.1 NCEP PrepBUFR data**

120 The baseline observation data are obtained from the National Centers for Environmental Prediction (NCEP)  
 121 Automated Data Processing (ADP) global upper air and surface weather observations that are available from the NCAR  
 122 Research Data Archive (NCAR RDA) (<https://rda.ucar.edu/datasets/ds337.0/>). These data are produced in the PrepBUFR  
 123 format for assimilation in the diverse NCEP NWP systems, and mainly consist of ground-based observations and satellite-  
 124 based wind retrievals. The ground-based observations include land and marine surface reports, aircraft reports, radiosonde,  
 125 and pilot balloon (pibal) measurements, which are transmitted via the Global Telecommunications System (GTS) coordinated  
 126 by the World Meteorological Organization (WMO). The satellite-based retrievals are provided from the National  
 127 Environmental Satellite Data and Information Service (NESDIS). They include oceanic wind derived from the Special Sensor  
 128 Microwave Imager (SSM/I) and upper wind from the LEO and GEO satellites. As the NCEP ADP dataset is provided in the  
 129 BUFR format, it must be converted to the data format available in the DART assimilation system, using the modules provided  
 130 in the DART data assimilation package.

### 131 3.2 AMSU-A data

132 AMSU-A is the microwave temperature sounder that is currently on board diverse sun-synchronous satellite  
 133 platforms e.g., MetOp satellites (MetOp-A, -B, and -C), three satellites of the National Oceanic and Atmospheric  
 134 Administration (NOAA), and the National Aeronautics and Space Administration (NASA) research satellite *Aqua*. These three  
 135 LEO satellite constellations provide near-global coverage, even in data assimilation that has a sub-daily assimilation window;  
 136 NOAA satellites circle in an early-morning orbit (around 0600 local time), MetOp satellites have a mid-morning orbit (around  
 137 0900 local time), and Aqua has an afternoon orbit (around 1300 local time). As a cross-track scanning sounder, the AMSU-A  
 138 instrument has a total of 15 channels that consist of 12 channels (AMSU-A channels 3–14) over the 50–58 GHz oxygen (O<sub>2</sub>)  
 139 absorption band and three window channels (AMSU-A channels 1, 2, and 15) at 23.8, 31.4, and 89 GHz. The instrument  
 140 measures 30 pixels in each swath with a spatial footprint size of 48 km in nadir. The channels over the O<sub>2</sub> absorption band  
 141 mainly provide information about the vertical structure of tropospheric and stratospheric temperature (Mo, 1999; Goldberg et  
 142 al., 2001). In this study, observations of AMSU-A instruments on board four LEO satellites (i.e., NOAA-19, Aqua, MetOp-A,  
 143 and MetOp-B) are assimilated within the DART data assimilation system.

144



145 **Figure 1.** Flowchart of the preprocessing system for AMSU-A brightness temperatures (BTs).  
 146

## 147 4 Preprocessing AMSU-A observations

148 Prior to assimilating the AMSU-A observations into DART, the AMSU-A observations should be passed through a  
149 preprocessing stage. Figure 1 shows the flowchart of the preprocessing stage for the AMSU-A observations as well as the  
150 DART assimilation step. In the preprocessing, three main steps are included: quality control, spatial thinning, and bias  
151 correction. Quality control consists of two sub-processes: outlier test and channel selection depending on the cloud condition  
152 and surface type. If the difference between the observed AMSU-A brightness temperature and the forward-modeled brightness  
153 temperature derived from the model background (6-h forecast) is larger than three times the square root of the sum of the  
154 observation error variance and the prior background error variance, the AMSU-A observation is not assimilated (called outlier  
155 test). As the prior background error variance is based on the ensemble spread, the larger the ensemble spread of the 6-h forecast,  
156 the more the AMSU-A observations are assimilated. More detailed information on the channel selection, spatial thinning, and  
157 bias correction process is described in sections 4.1, 4.2, and 4.3, respectively.

### 158 4.1 Channel selection for the cloud condition and surface type

159 As each AMSU-A channel has distinct spectral characteristics, it is necessary to carefully choose the channels to be  
160 assimilated in the DART data assimilation system. First, the three AMSU-A channels at 23.8, 31.4, and 89 GHz (i.e., channels  
161 1, 2, and 15), distributed over the window region of the microwave spectrum, are not assimilated. These three window channels  
162 are mostly affected by the emitted radiances from the surface under clear-sky conditions, so there is almost no information  
163 about the atmosphere. However, AMSU-A channels 1 (23.8 GHz) and 2 (31.4 GHz) are highly sensitive to clouds, so they are  
164 used for the quality control in which clouds are detected. In addition, even though the AMSU-A channels 3 (50.3 GHz) and 4  
165 (52.8 GHz) are located over the O<sub>2</sub> absorption band used for the temperature sounding, they have a strong sensitivity to the  
166 surface, so they are not used in DART. Considering that the upper parts of the weighting function of AMSU-A channels 12  
167 (57.29±0.322±0.022 GHz), 13 (57.29±0.322±0.010 GHz), and 14 (57.29±0.322±0.0045 GHz) are above the top of the  
168 atmosphere (i.e., 3.6 hPa) in the CAM6, these three channels are also removed to prevent vertical interpolation errors that may  
169 occur in the forward modeling using the RTM. This leaves channels 5-11 (53.596±0.115, 54.4, 54.94, 55.5, 57.29, 57.29±0.217,  
170 and 57.29±0.322±0.048 GHz) as the ones which may be assimilated.

171 As this study aims to assimilate the AMSU-A observations under the clear-sky condition, the cloud-affected channels  
172 are filtered out in the quality control step. In other words, the tropospheric channels (channels 5–7) whose peak of the weighting  
173 function is below 200 hPa are rejected if the AMSU-A pixel is determined to be a cloud-affected pixel. To determine this, we  
174 calculate the cloud liquid water (CLW) derived from observations of AMSU-A channels 1 and 2 over the ocean, using the  
175 retrieval methodology suggested by Grody et al. (2001). The CLW is defined as follows:

$$176 \text{CLW} = \cos\theta [D_0 + 0.754 \ln(285.0 - BT_{23}) - 2.265 \ln(285.0 - BT_{31})] \quad (1)$$

$$177 D_0 = 8.240 - (2.622 - 1.846 \cos\theta) \cos\theta \quad (2)$$

181 where  $\theta$  is the satellite viewing zenith angle.  $BT_{23}$  and  $BT_{31}$  are the brightness temperature of AMSU-A channels 1 and 2,  
182 respectively. If the retrieved CLW is larger than 0.2 mm, the AMSU-A pixel is judged to be cloud-contaminated, then the three  
183 tropospheric channels (channels 5–7) are rejected.

184 In this study, seven candidate AMSU-A channels (i.e., channels 5–11) are assimilated differently, depending on the  
185 surface type. Channels 5, 6, and 7 are the main tropospheric channels. Their weighting functions peak below 200 hPa, but also  
186 have a bit of sensitivity to the surface because of the broad vertical shape of the weighting functions. Thus, the quality of the  
187 analysis can be degraded by assimilating the three tropospheric channels over the land and sea-ice types whose surface

188 information (e.g., surface temperature and surface spectral emissivity) is uncertain. For this reason, AMSU-A channels 5–7 are  
 189 not assimilated over the land and sea ice. To identify sea-ice area, the sea-ice index (SII) is retrieved from observations of  
 190 AMSU-A channels 1 and 3 over the high latitude region (poleward of 50 degrees), using the retrieval algorithm suggested by  
 191 Grody et al. (1999). The SII is derived as follows:

$$192 \quad \text{SII} = 2.85 + 0.20 \text{ BT}_{23} - 0.028 \text{ BT}_{50} \quad (3)$$

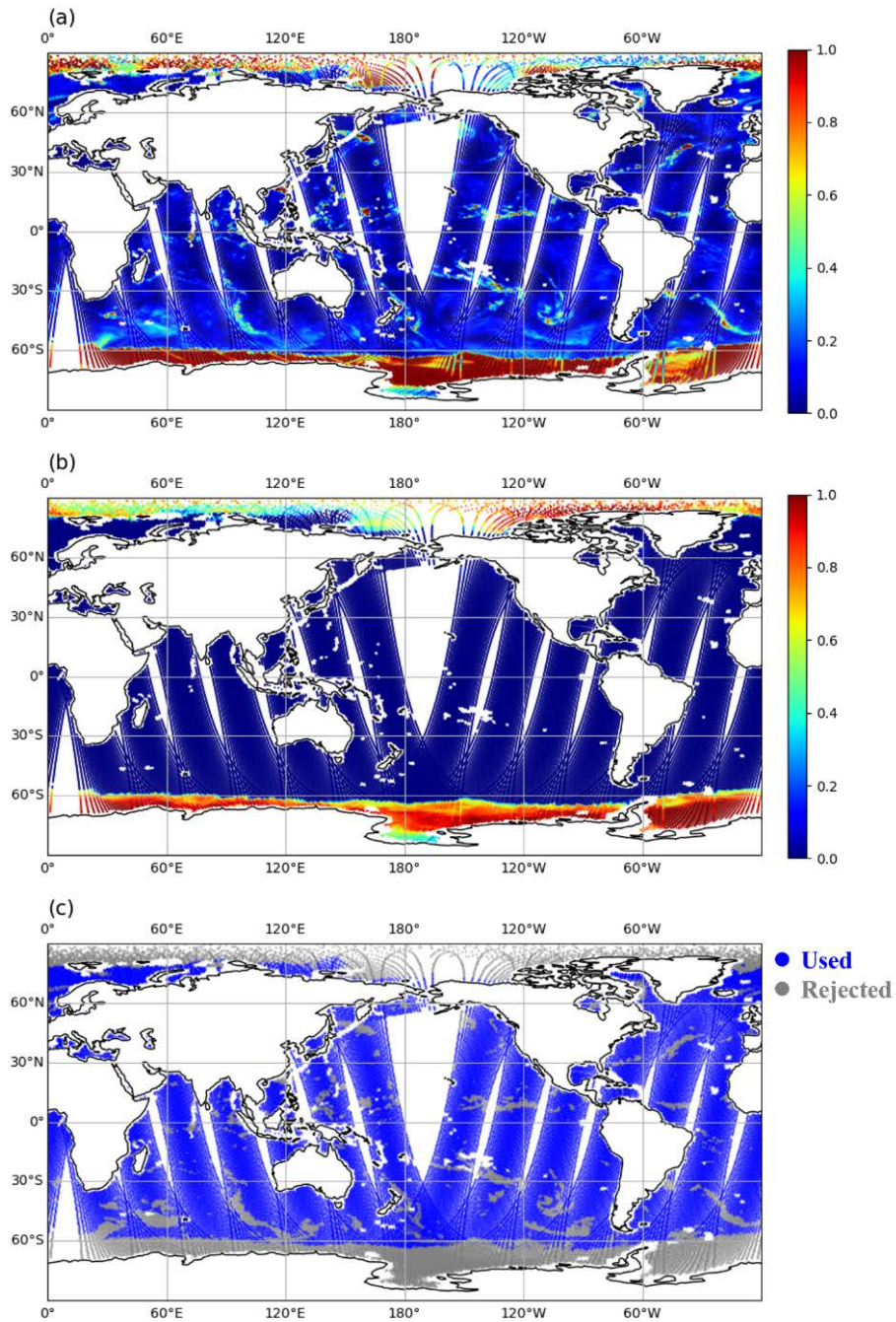
193  
 194  
 195 where  $\text{BT}_{50}$  is the brightness temperature of AMSU-A channel 3. Three tropospheric channels are turned off if the SII is larger  
 196 than 0.1 in the latitudes beyond 50 degrees. However, as the surface information over the ocean is relatively reliable, seven  
 197 candidate AMSU-A channels are assimilated under the clear-sky condition. The AMSU-A channel list for DART is summarized  
 198 in Table 1.

199  
 200 **Table 1.** AMSU-A channel list for the DART data assimilation.

Satellite platform	Type	CH5	CH6	CH7	CH8	CH9	CH10	CH11
Aqua	Land/Sea-ice		X		O	O	O	O
	Ocean	N/A*	O	N/A	O	O	O	O
	Cloud		X		O	O	O	O
NOAA-19	Land/Sea-ice	X	X	X		O	O	O
	Ocean	O	O	O	N/A	O	O	O
	Cloud	X	X	X		O	O	O
MetOp-A	Land/Sea-ice	X	X			O	O	O
	Ocean	O	O	N/A	N/A	O	O	O
	Cloud	X	X			O	O	O
MetOp-B	Land/Sea-ice	X	X	X	O	O	O	O
	Ocean	O	O	O	O	O	O	O
	Cloud	X	X	X	O	O	O	O

201 \*N/A: not available due to the malfunction in August and September 2014. O: assimilated. X: excluded.

202  
 203 As an example, Figure 2a and b presents the spatial distribution of the CLW and the SII retrieved from AMSU-A on  
 204 board NOAA-19 on 12 August 2014. It is found that many regions over the ocean are covered by cloud-related systems (CLW  
 205 > 0.2 mm) and also sea-ice (SII > 0.1) exists near the north and south pole regions. Observations of AMSU-A channel 5 over  
 206 the cloud region and sea-ice areas are rejected (Fig. 2c). The channel selection process is also applied to the other two AMSU-  
 207 A channels (channels 6 and 7) which are likely affected by clouds and sea ice. In the pre-trial runs, it was found that the analysis  
 208 quality is degraded if the AMSU-A observations are assimilated over Antarctica during the Southern Hemisphere winter season.  
 209 It seems to be due to the complex topography of the Antarctic continent, extreme cold weather conditions, and large errors in  
 210 the numerical model. Thus, AMSU-A observations are not used over the high latitude region (> 60°S) during the Southern  
 211 Hemisphere winter season, in order to prevent the degradation of the analysis quality.



212 **Figure 2.** Spatial distribution of (a) cloud liquid water (CLW, mm), (b) sea-ice index (SII) retrieved from AMSU-A observations, and (c)  
 213 quality flag of AMSU-A channel 5 (53.6 GHz) from NOAA-19 on 12 August 2014.  
 214

## 215 4.2 Spatial thinning

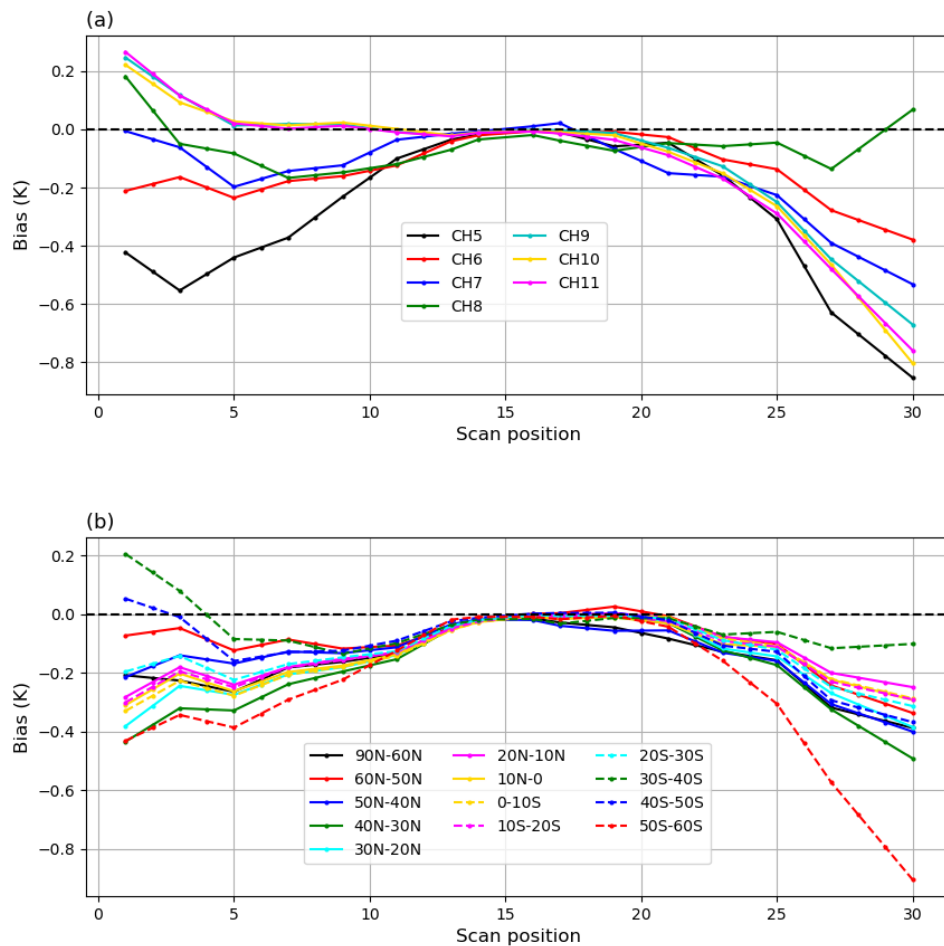
216 In addition to the inter-channel error correlation (refer to section 5), spatial error correlation between the observations  
 217 at a close distance also exists due to different representativeness of the observed radiances and the model state, and the  
 218 uncertain quality control process such as cloud detection (Ochotta et al., 2005; Bormann and Bauer, 2010). Thus, the analysis  
 219 is likely to be sub-optimized if highly dense observations are assimilated without considering the spatial error correlations. A  
 220 common treatment to counteract the spatial error correlation is spatial thinning which is widely used in data assimilation  
 221 systems operated by the NWP centers. To choose the optimal spatial thinning distance, we performed four extra assimilation  
 222 runs in which different spatial thinning distance (i.e., 96 km, 192 km, 288 km and 384 km) was applied. To choose the optimal  
 223 spatial thinning distance, we performed four extra assimilation runs in which different spatial thinning distance (i.e., 96 km,  
 224 192 km, 288 km and 384 km) was applied. Except for the spatial thinning distance, these pre-trial runs were set up with the  
 225 same assimilation factors, i.e., the estimated bias correction coefficients (refer to section 4.3), the estimated observation errors

226 (refer to section 5), and the localization half-width of 0.075 (refer to section 6). These distances are multiples of the AMSU-A  
 227 field of view (FOV) footprint size (~48 km in nadir). The thinning interval of 288 km resulted in the largest analysis impact,  
 228 so that distance was used to thin the observations in this study.

### 229 4.3 Bias correction

230 The biases mainly come from systematic errors: instrument calibration errors, inaccuracies of the RTM, and  
 231 uncertain preprocessing (e.g. cloud detection errors). The biases tend to depend on time-of-day and on the season as well as  
 232 the instrument scan angle and air mass. While random errors are considered by defining the observation errors used in the  
 233 assimilation process, the biases should be removed before assimilating the satellite observations. In these experiments, the  
 234 biases are estimated using the time averaged departures between the observed radiances and the simulated radiances from the  
 235 spatiotemporally collocated model field (background), because of the absence of reference data suitable to compare the satellite  
 236 observations (Scheck et al., 2018). The use of the simulated radiances from the model background (i.e., 6-h forecast) may be  
 237 questionable because the model background could be biased. However, it is effectively impossible to find sufficient reference  
 238 observations for comparing with these satellite observations, so the biases are made using the departures between the observed  
 239 radiances and the model simulated radiances. To estimate the systematic biases coming from diverse error sources, in this study,  
 240 two bias correction processes are performed separately: scan-bias correction and air-mass-bias correction, using the statistical  
 241 bias correction methods suggested by Harris and Kelly (2002).

242



243 **Figure 3.** (a) Globally averaged, residual scan bias of AMSU-A channels 5–11 and (b) the regionally averaged, residual scan bias depending  
 244 on 13 latitude bands for AMSU-A channel 6 on board MetOp-B during the period from 11 August to 25 August 2014.  
 245  
 246

247 As a cross-track microwave sounder, the AMSU-A scans 30 FOVs per scan line, which are distributed symmetrically  
 248 about the nadir. The scan angles of 30 FOVs range between  $\pm 48.33^\circ$ . Thus, the observed radiance varies depending on the scan



249 angle even though the observation point is the same. The variation of AMSU-A radiance is due to the change in the optical  
 250 path length between the earth and the satellite instrument, called the limb effect. The variation of radiance along with the scan  
 251 angle can be simulated in the RTTOV embedded in DART. However, the mean first-guess departures between the AMSU-A  
 252 observed radiances and forward-modeled radiances still increase with an increasing scan angle on the center of two near-nadir  
 253 FOVs (15 and 16) (Fig. 3a), meaning that the residual scan-angle-dependent biases exist for each AMSU-A channel. Thus, the  
 254 scan-bias correction is required to correct the residual scan bias for each AMSU-A channel. In this study, the scan-bias  
 255 correction is performed using the pre-computed residual scan bias for each AMSU-A channel. There are two steps to estimate  
 256 the residual scan bias for AMSU-A channels assimilated. First, the mean bias of the departure between the AMSU-A observed  
 257 radiances and forward-modeled radiances for each FOV is made with the data assimilation results derived from the pre-trial  
 258 run. The pre-trial run was set up with the spatial thinning of 96 km (refer to section 4.2) and the default localization half-width  
 259 (0.15, refer to section 6). The instrument noise errors were used as the observation errors within DART. Second, as the scan  
 260 bias derived from the departures between the observed radiances and forward-modeled radiances likely includes the air-mass  
 261 bias, the averaged residual scan bias is obtained by removing the mean bias of two near-nadir FOVs (15 and 16) from the bias  
 262 for each FOV (1–30). In addition, as shown in Fig. 3b, it is also found that the residual scan biases have different patterns  
 263 depending on the latitude band for AMSU-A channel 6 (not shown for other channels), suggesting that the use of globally  
 264 averaged scan bias is likely to deteriorate the quality of AMSU-A data assimilation. Thus, the residual scan ( $b^{scan}$ ) bias for  
 265 each AMSU-A channel is subdivided into 14 latitude bands as follows:

$$266 \quad b_i^{scan}(\theta, \phi) = [y - H(x_b)]_i(\theta, \phi) - [y - H(x_b)]_i(\theta = 0, \phi) \quad (4)$$

267 where the subscript  $i$  denotes the AMSU-A channel number ( $i=1, 2, \dots, 15$ ),  $\theta$  is the satellite scan angle,  $\phi$  is the latitude band  
 268 at an interval of 10 degrees in the latitudes below 60 degrees and 30 degrees in the latitudes beyond 60 degrees,  $y$  is the AMSU-  
 269 A radiance,  $x_b$  is the background model state, and  $H$  is the observation operator. Prior to the air-mass-bias correction, the  
 270 observed brightness temperatures of each AMSU-A channel are corrected using the estimated scan bias coefficients.

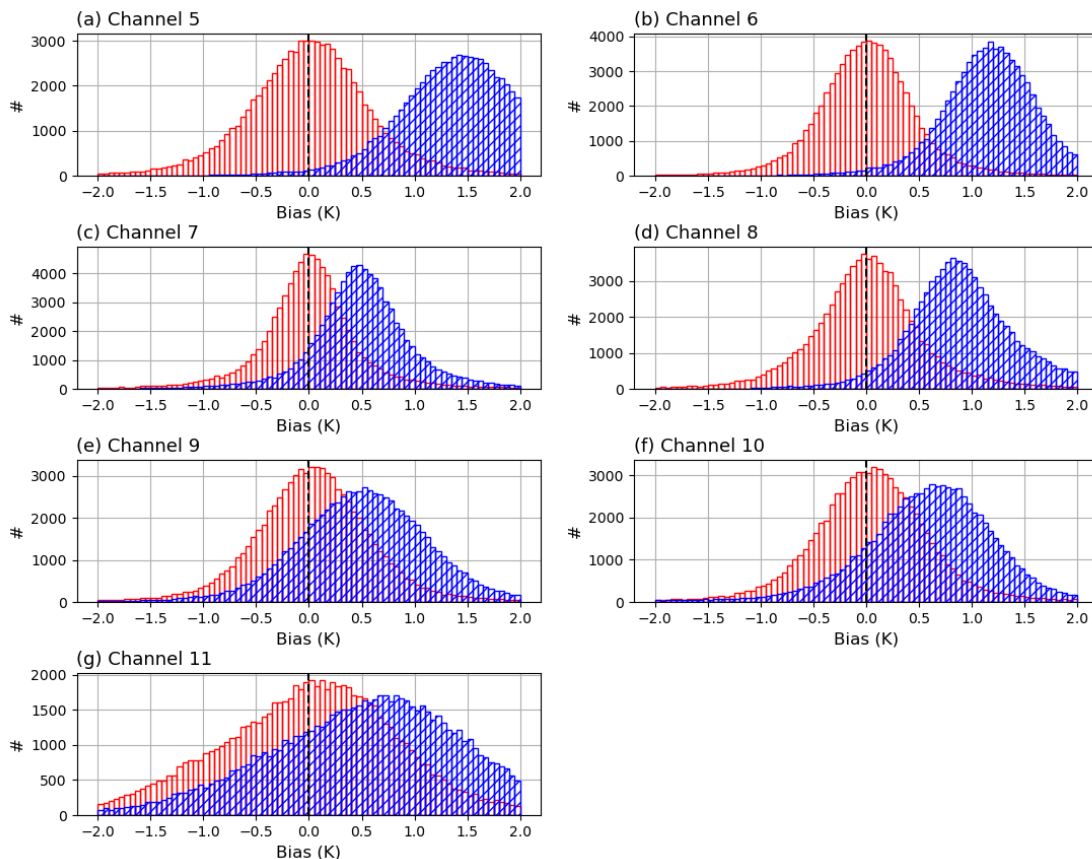
271 The air-mass bias ( $b^{airmass}$ ) is predicted using the multivariate regression method. The biases are mainly due to  
 272 uncertainties in the RTM, which tend to vary with the air mass and surface characteristics. The predictors, used in the regression  
 273 method, come from the model variables (i.e., 1000–300 hPa thickness, 200–50 hPa thickness, and surface temperature) that  
 274 include information on air mass and surface characteristics. The predictors regress to the first-guess departure between the  
 275 satellite radiances and forward-modeled radiances as follows:

$$276 \quad b_i^{airmass} = \beta_{i,0} + \sum_{j=1}^N \beta_{i,j} p_{i,j} \quad (5)$$

277 where  $\beta_{i,0}$  indicates the constant component of bias  $b_i$ , and  $\beta_{i,j}$  are the bias correction coefficients of the predictor  $p_{i,j}$ . The  
 278 subscripts  $i$  and  $j$  denote the AMSU-A channel number and the predictor number (i.e.,  $j = 1, 2, \dots, N$ ), respectively.

279 For the tropospheric AMSU-A channels (channels 5–7), the air mass bias is estimated with two model variables (i.e.,  
 280 1000–300 hPa thickness and surface temperature), because the peak of the channel weighting function is positioned below the  
 281 200 hPa pressure level, and these channels have a bit of sensitivity to the surface. However, 200–50 hPa thickness is only  
 282 employed for other upper-tropospheric and stratospheric AMSU-A channels (channels 8–11) whose peak of the weighting  
 283 function is above 200 hPa. As the biases fluctuate with time, it is reasonable to update the regression coefficients and an  
 284 intercept point periodically, rather than using the climatological-based coefficients that are estimated using the long-term model  
 285 outputs. In this study, at each data assimilation cycle, the regression coefficients and an intercept point for each AMSU-A  
 286 channel are computed using DART outputs for the last four cycles and then used to predict the air-mass biases. As shown in  
 287  
 288  
 289  
 290

291 Fig. 4, the histograms of the first-guess departures of the MetOp-B channels 5–11 show a positive bias and a Gaussian  
 292 distribution if the AMSU-A observations are not bias-corrected. In particular, channels 5 and 6 have a large positive bias of  
 293 1.0–1.5K. However, the positive biases are almost removed through the bias correction process, meaning that the bias  
 294 correction scheme works well (Table 2).  
 295



296  
 297 **Figure 4.** Histogram of the first-guess departures between the observations of the MetOp-B AMSU-A channels 5–11 and the corresponding  
 298 model background (6-h forecast). Colors indicate the results before the bias correction (hatched blue) and after the bias correction,  
 299 respectively.  
 300

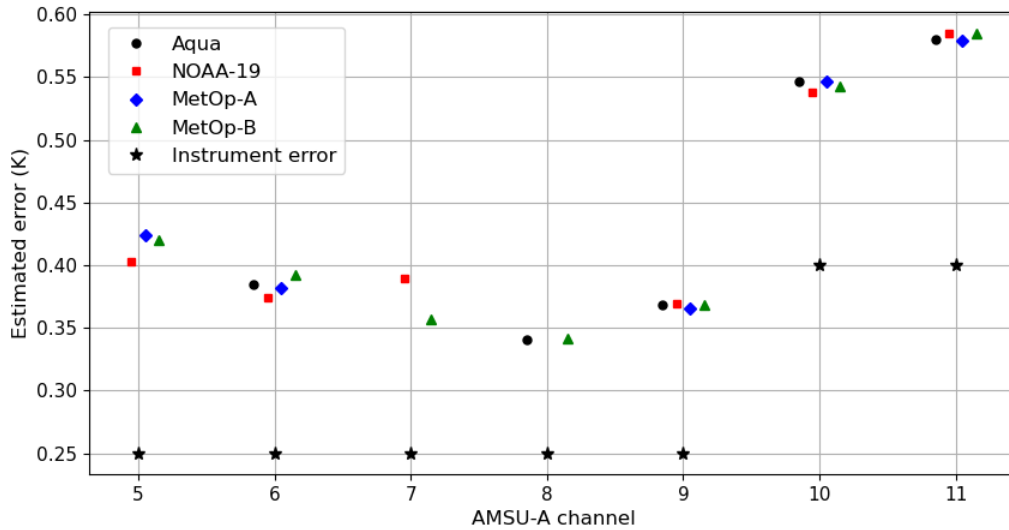
301 **Table 2.** Mean biases and standard deviations of the first-guess departures (O-B) for MetOp-B AMSU-A channels before and after the bias  
 302 correction.

O-B	Bias correction	CH5	CH6	CH7	CH8	CH9	CH10	CH11
Bias	X	1.518	1.181	0.514	0.937	0.514	0.590	0.612
	O	0.0005	0.002	0.003	0.014	0.033	0.028	0.010
STDDEV	X	0.677	0.489	0.521	0.572	0.639	0.688	1.052
	O	0.627	0.482	0.494	0.554	0.580	0.642	0.966

### 303 5 AMSU-A observation errors

304 As well as the model background error, the observation errors play an important role in determining the weight of  
 305 the observations in the data assimilation system. Thus, it is an important step to define the observation errors so that the  
 306 observations are suitably blended with the model background, which is a 6-hour forecast derived from the CAM6, in order to  
 307 provide the optimal initial condition to the numerical model. In this study, a diagonal observation error covariance matrix is  
 308 used for the AMSU-A channels, meaning that the inter-channel error correlation is not considered. In fact, the use of the  
 309 diagonal observation error covariance matrix may be problematic because the inter-channel error correlation definitely exists

310 for the infrared and microwave sounders (Bormann and Bauer, 2010; Stewart et al., 2014; Weston et al., 2014; Campbell et al.,  
 311 2017). Unfortunately, the recent version of DART (version 9.11.13) does not support the use of a full observation error  
 312 covariance matrix in which the diagonal and off-diagonal components are fully defined. For this reason, the diagonal  
 313 observation errors are empirically inflated to counteract the effect of error correlation between different AMSU-A channels. In  
 314 other words, the inflated diagonal observation errors take account of the inter-channel error correlation as well.  
 315



316 **Figure 5.** Estimated observation errors (K) for AMSU-A channels on board Aqua (black: circle), NOAA-19 (red: square), MetOp-A (blue:  
 317 diamond), and MetOp-B (green: triangle) satellite platforms. Black asterisks indicate the instrument noise errors for AMSU-A channels.  
 318  
 319

320 To estimate the diagonal components (called variances) of the observation error covariance matrix ( $R$ ) for AMSU-A  
 321 channels, we use a diagnostic procedure suggested by Desroziers et al. (2005) in which the error variances are made with two  
 322 departures, i.e., the background innovation (O-B) between the observation ( $y$ ) and the model background ( $x_b$ ) and the analysis  
 323 innovation (O-A) between the observation and the model analysis ( $x_a$ ), using the expression in Eq. (6).  
 324

$$R = E[\{y - H(x_b)\} \{y - H(x_a)\}^T] \quad (6)$$

325  
 326 where  $E$  is the statistical expectation operator and the superscript “T” indicates the matrix transpose. To compute the  
 327 observation error variances of AMSU-A channels on board four satellite platforms (i.e., Aqua, NOAA-19, MetOp-A, and  
 328 MetOp-B), the background and analysis innovations were derived from the pre-trial run that was conducted from 25 August  
 329 to 30 September 2014. In the pre-trial run, instrument noise errors were simply used as the observation errors. The pre-trial  
 330 run was set up with the default localization half-width (0.15, refer to section 6), the spatial thinning of 96 km (refer to section  
 331 4.2), and the bias correction scheme (refer to section 4.3). ~~In the pre-trial run, the instrument noise errors were initially used~~  
 332 ~~as the observation errors within DART.~~ Then, the observation error variances were estimated using the Eq. (6).  
 333

334 As the surface-sensitive channels and upper-stratospheric channels are not assimilated in this study (see section 4.1),  
 335 Figure 5 shows the observation errors of seven AMSU-A channels (channels 5–11) as well as the instrument noise errors  
 336 employed in the pre-trial run. As some channels (i.e., channels 5 and 7 for Aqua, channel 8 for NOAA-19, and channels 7 and  
 337 8 for MetOp-A) malfunctioned during the trial period (11 August – 30 September 2014), the errors for these channels were not  
 338 needed or estimated. The estimated errors are larger than the instrument noise errors because various error sources (e.g., the  
 339 radiative transfer modeling errors, representative errors, and systematic errors) are considered as well as the instrument noise  
 340 errors. The estimated errors for the tropospheric and upper-tropospheric channels (channels 5–9) are smaller than the errors  
 341 for the stratospheric channels (channels 10–11). This error pattern is also presented for the instrument noise errors. As

342 aforementioned, the estimated observation errors were inflated by a factor of two that was empirically estimated by the multiple  
343 pre-trial runs, in order to counteract the inter-channel error correlation. Then, the inflated observation errors, two times the  
344 estimated observation errors, were employed for the trial experiments aiming at assessing the analysis impact of assimilating  
345 the AMSU-A observations.

## 346 **6 Trial experiment design**

347 To diagnose the analysis impact of assimilating the AMSU-A observations into the DART global data assimilation  
348 system, two assimilation experiments were conducted: (a) a control run (CNTL) where the conventional observations (i.e.,  
349 ground-based observations and satellite-derived winds) were assimilated, and (b) “AMSU-A run”, where the AMSU-A  
350 observations from four LEO satellite platforms (i.e., Aqua, NOAA-19, MetOp-A, and MetOp-B) were assimilated as well as  
351 the conventional data that were assimilated in the CNTL run. For the AMSU-A run, the developed preprocessing steps (e.g.,  
352 channel selection, thinning, and bias correction) were applied to the AMSU-A observed radiances and then the pre-computed  
353 AMSU-A observation errors were employed in the DART data assimilation process.

354 For two trial runs, available observation data were assimilated within a 6-h assimilation window from -3 to +3 h  
355 centered at the nominal analysis time (0000, 0600, 1200, and 1800 UTC). All trial runs were carried out four times a day for  
356 the trial period from 0000UTC 11 August to 1800UTC 30 September 2014. The CAM6 forecast model was run with a nominal  
357 1° horizontal resolution (1.25° in longitude and 0.95° in latitude) and 32 vertical levels. The initial ensembles that are available  
358 at the NCAR RDA (<https://rda.ucar.edu/datasets/ds345.0/>) were obtained from the DART reanalysis. To adjust the effect of  
359 initial ensembles, a two-week spin-up period (0000UTC 11 August to 1800UTC 24 August 2014) was included in the trial  
360 period. In this study, the ensemble adjustment Kalman filter (EAKF) is applied, which is a variation of the EnKF (Anderson,  
361 2001). Twenty ensemble members were integrated to compute the flow-dependent background error covariance and the  
362 correlation between the DART state variables and observations.

363 All EnKF-based assimilation techniques have the sampling error that is induced by the limited size of the ensemble.  
364 In particular, the sampling error is likely to be large when the absolute value of correlation between the DART state variables  
365 and the observations is small. To remove the spurious correlation induced by limited ensemble size in DART, the correlation  
366 is multiplied by a localization factor that decreases from 1 to 0 with the physical distance between the model state variables  
367 and the observations. In DART, the localization half-width can be user-defined, which is half of the distance to where the  
368 localization factor is zero. To determine the localization half-width, three extra assimilation experiments were run with different  
369 half-widths (i.e., 0.15, 0.075, and 0.0375). Except for the localization half-width, the assimilation experiments were set up  
370 with the spatial thinning of 96 km (refer to section 4.2), the bias correction scheme (refer to section 4.3), and the estimated  
371 observation errors (refer to section 5). As the largest analysis impact was made with the half-width of 0.075, the  
372 horizontal/vertical localization half-width of 0.075 radians was employed to prevent the use of erroneous correlation. However,  
373 as the model top height is quite lower than the Earth’s horizontal scale, the localization half-width in the vertical is normalized  
374 by the user-defined scale height, which is equivalent to one radian. In DART, the difference in scale height between the model  
375 top (360 Pa) and the standard surface pressure (101325 Pa) is 5.73. In this study, the normalization scale height of 1.5, a default  
376 value in DART, was used, which is assumed to be equal to one radian. Thus, the localization half-width of 0.075 radians is  
377 converted into the scale height of 0.11, meaning that the localization cutoff can be an ellipsoid that is flat horizontally. In  
378 addition to the reduction of localization half-width (compared to the default value of 0.15), the sampling error correction  
379 algorithm was applied, which uses pre-defined information about the correlation between the model state variables and the  
380 observations as a function of ensemble size. Detailed information on the sampling error correction algorithm is described in  
381 Anderson (2012).

382 The EnKF technique has a risk of underestimation of the ensemble spread, meaning that the ensemble estimates are

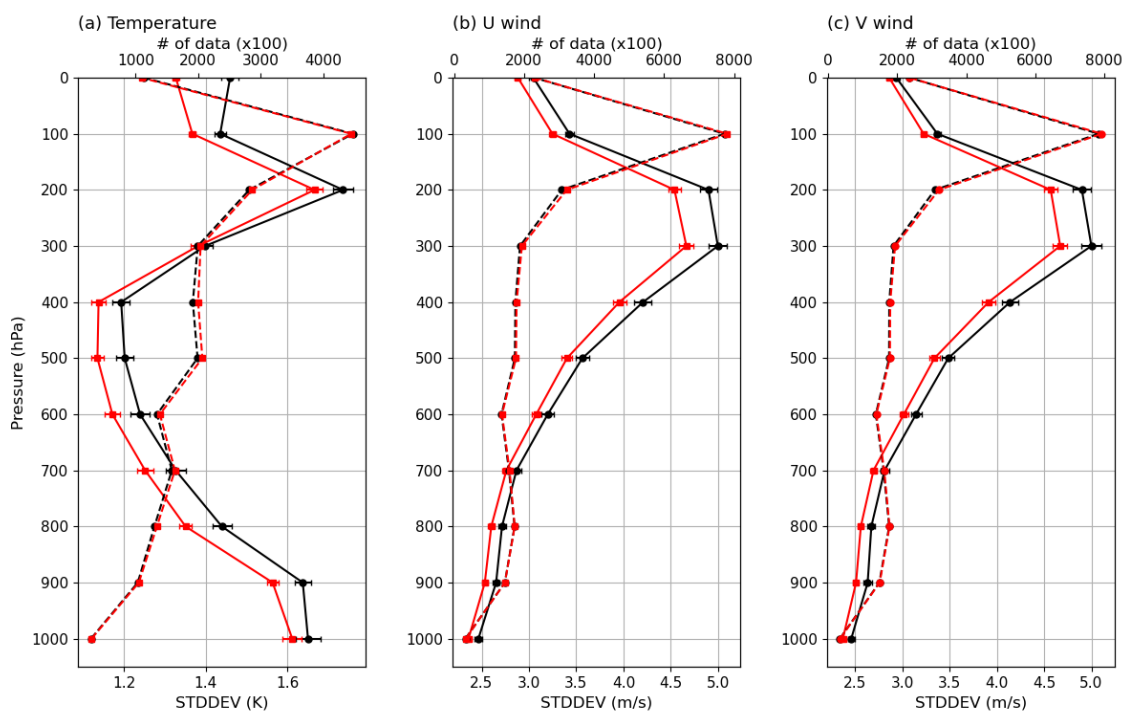
383 too confident. If the ensemble spread becomes too small, the observation data are ignored in the data assimilation process,  
 384 resulting in an ensemble collapse (Anderson et al., 2009; El Gharamti et al., 2019). To mitigate the underestimation issue of  
 385 the ensemble spread, the uncertainty in the ensemble estimate is inflated by linearly moving each ensemble member away  
 386 from the ensemble mean. It means that the standard deviation of the ensemble spread increases by applying the inflation value  
 387 in a way that the ensemble mean is unchanged. In DART, the ensemble spread varies spatiotemporally, as a function of the  
 388 evolving observation network and the chosen inflation algorithm. These experiments use a spatiotemporally varying inflation  
 389 algorithm with a Gaussian distribution. More detailed information on the inflation algorithm adopted in DART is presented in  
 390 El Gharamti et al. (2019).

## 391 7 Results

### 392 7.1 Assessment of first-guess departure and analysis departure

393 As the same conventional radiosonde measurements were assimilated in the two trial runs (i.e., CNTL and AMSU-  
 394 A), the first-guess departure statistics between the radiosonde measurements and the spatiotemporally-located background  
 395 states (6-h forecast) can be used to assess the impact of the AMSU-A observations to the short-range forecast. Figure 6 shows  
 396 the vertical structure of the standard deviation (STDDEV) of the first-guess departure from the radiosonde temperature, zonal  
 397 wind, and meridional wind as well as the number of the radiosonde measurements used.

398



399  
 400  
 401  
 402  
 403  
 404

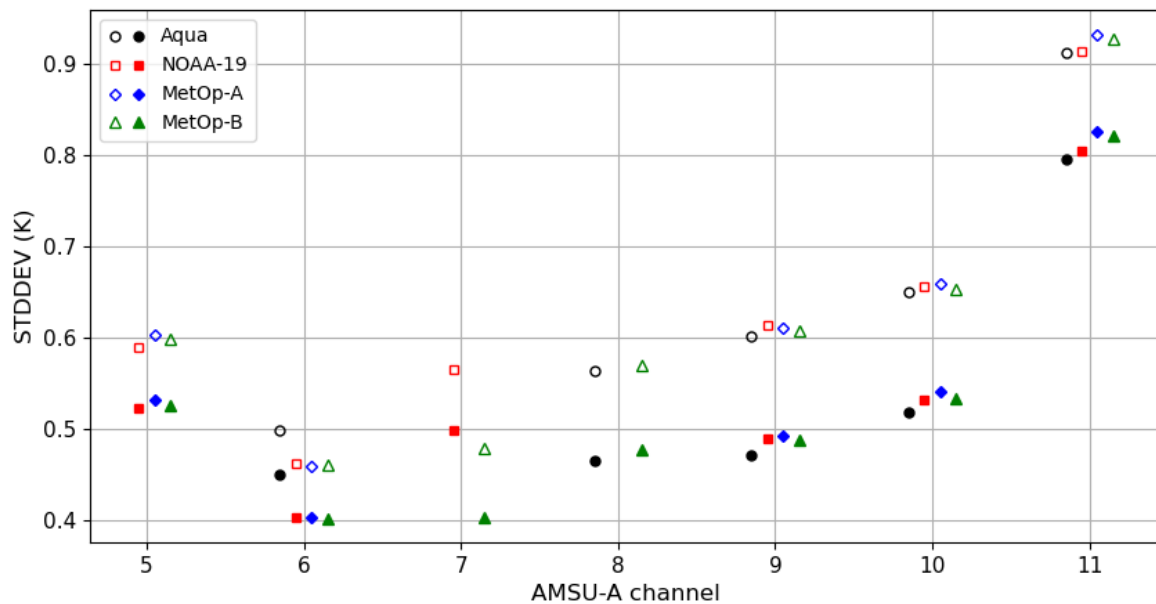
**Figure 6.** The standard deviation (STDDEV) of the first-guess departures for the radiosonde (a) temperature, (b) zonal wind, and (c) meridional wind for the control (CNTL run: circle symbol and black line) and experiment (AMSU-A run: square symbol and red line) runs. Solid and dashed lines indicate the STDDEV and the number (top axis) of radiosonde measurements assimilated, respectively. The 99% confidence intervals are indicated by the horizontal black lines.

405 For the temperature, the first-guess departure errors are significantly reduced below 300 hPa for the AMSU-A runs  
 406 as compared with the errors for the CNTL run (Fig. 6a). Because the AMSU-A channels provide vertical information about  
 407 the air temperature, the temperature error reduction is the direct impact derived by assimilating the AMSU-A observations in  
 408 the AMSU-A run. In addition to the radiosonde temperature, the first-guess departure errors decrease for the two wind  
 409 components (i.e., zonal and meridional winds) (Fig. 6b and c). In particular, the STDDEVs of the two winds at the 300 hPa

410 level are reduced by up to about 4.7m/s in the AMSU-A run, compared to the error of about 5.1m/s for the CNTL run. As the  
 411 model background error covariance includes the multivariate correlation between different model parameters (e.g., temperature  
 412 and winds), a change in one model parameter can change another model parameter in the assimilation process. In addition,  
 413 model parameters are linked in the governing equations and the physical parameterizations, which are embedded in the CAM6.  
 414 That is, the change in one parameter results in the adjustment of another parameter in the model time integration. Thus, the  
 415 error reduction of the wind components is the indirect impact of the improved temperature field by assimilating the AMSU-A  
 416 observations.

417 In addition to the first-guess departure analysis of radiosonde, the assimilation impact of the AMSU-A observations  
 418 can be diagnosed by comparing the first-guess departures of the AMSU-A with the analysis departures between the AMSU-A  
 419 observations and the model analysis state. In general, if the observations are successfully assimilated, the STDDEV of the  
 420 analysis departure is smaller than that of the first-guess departure, because the background fields are improved by assimilating  
 421 the observations. As shown in Fig. 7, the STDDEVs of the analysis departure are significantly smaller than that of the first-  
 422 guess departure for AMSU-A assimilated channels (channels 5–11) regardless of the satellite platforms, meaning that the  
 423 AMSU-A observations have a positive analysis impact. In particular, the gap between the STDDEVs of two departures is large  
 424 for the stratospheric AMSU-A channels (channels 9–11).

425



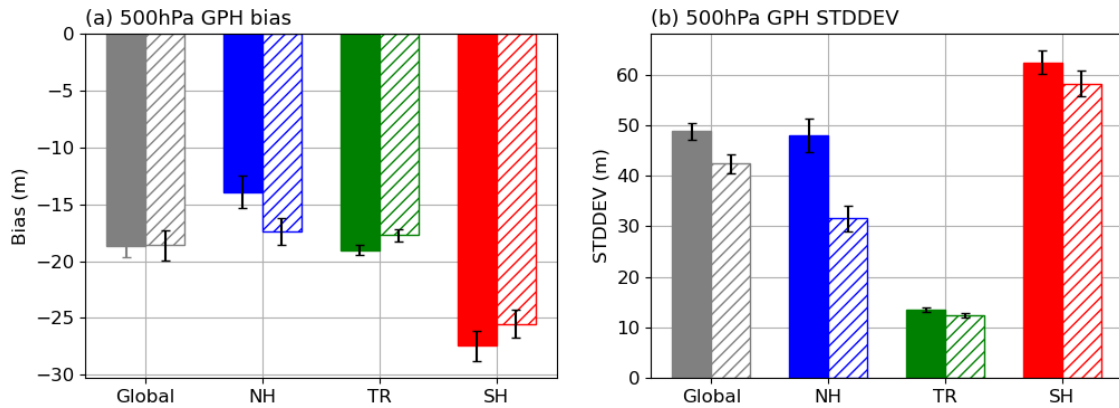
426

427 **Figure 7.** The standard deviations (STDDEVs) of the first-guess departure (unfilled symbols) and analysis departure (filled symbols) for  
 428 AMSU-A channels on board Aqua (black: circle), NOAA-19 (red: square), MetOp-A (blue: diamond), and MetOp-B (green: triangle)  
 429 satellites.

## 430 7.2 Analysis impact of AMSU-A observations

431 To assess the impact of the AMSU-A observations on the analysis derived from the DART data assimilation system,  
 432 the analysis errors are computed between the DART analysis and the European Centre for Medium-Range Weather Forecasts  
 433 (ECMWF) reanalysis version 5 (ERA5) as the reference data. As the ERA5 is made through the assimilation of all available  
 434 observation data in the ECMWF data assimilation system and provides consistent maps without spatial gaps, the ERA5 is  
 435 employed to assess the model-derived output. For four primary atmospheric parameters (i.e., 500 hPa geopotential height,  
 436 temperature, zonal wind, and meridional wind), the departures between the DART ensemble-mean analysis and the ERA5 are  
 437 computed. Then bias and standard deviation are derived from the long-term departures. In particular, the error of 500 hPa  
 438 geopotential height is widely used to assess the overall performance of the model-derived output, because large-scale  
 439 atmospheric motion in the middle troposphere (500 hPa) is closely linked with lower-level atmospheric motion.

440 Figure 8 describes the mean bias and STDDEV of 500 hPa geopotential height for the CNTL and AMSU-A run,  
 441 depending on the latitudinal regions. Detailed error values are described in Table 3. For two trial runs, overall negative mean  
 442 bias occurs, reaching up to about -18m. However, the bias difference varies depending on the latitudinal regions. Over the  
 443 Northern Hemisphere (30°N–90°N), the AMSU-A run has a larger negative bias than the bias for the CNTL run. However,  
 444 over the tropics (30°S–30°N) and Southern Hemisphere (30°S–90°S), the CNTL run has a larger negative bias than the bias  
 445 for the AMSU-A run. Thus, similar global mean bias (about -18m) for two trial runs is caused by the offsetting between  
 446 regionally different bias patterns.



447 **Figure 8.** (a) Mean bias and (b) standard deviation (STDDEV) of [the analysis of](#) 500 hPa geopotential height over the global (grey), Northern  
 448 Hemisphere (NH: blue), tropics (TR: green), and Southern Hemisphere (SH: red), derived against the ERA5 reanalysis. Filled and hatched  
 449 bars indicate the results for the control (CNTL) and experiment (AMSU-A) run, respectively. The 99% confidence intervals are indicated by  
 450 the vertical black lines.  
 451  
 452

453 Considering that the geopotential height is a primary function of the average air temperature between the surface  
 454 and the pressure level, we assumed that the model temperature has a cold bias at least below the 500 hPa pressure level. As  
 455 expected, it is found that a negative bias is presented in the temperature field for both two trial runs (not shown). In addition,  
 456 as shown in Fig. 9, the first-guess departure of the radiosonde temperature for the two trial runs has large positive values,  
 457 implying that a cold bias exists in the model temperature fields (6-h forecast). In Raeder et al. (2021), it was noted that the  
 458 CAM6/DART-derived reanalysis has a cold bias in the troposphere. However, it is still unclear the reason why the CAM6-  
 459 based temperature fields have a cold bias. The bias issue in CAM6 will be an interesting study in future work.  
 460

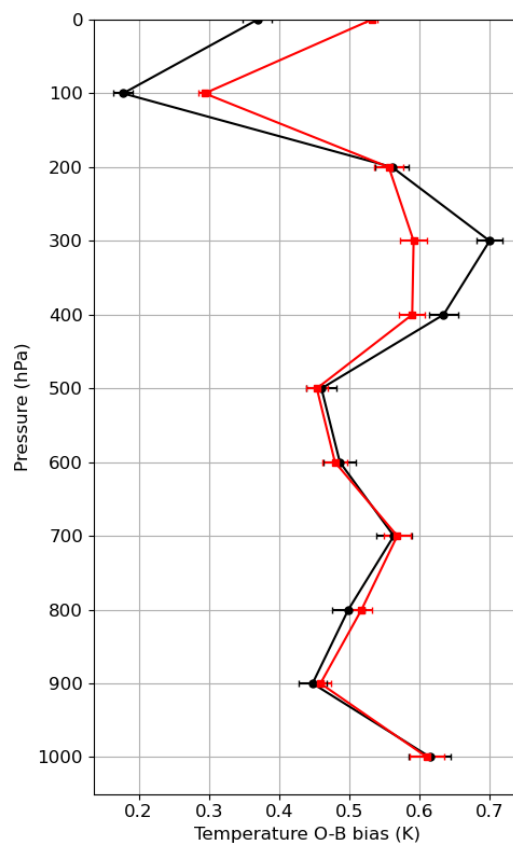
461 **Table 3.** Error statistics of 500 hPa geopotential height (m) for the control (CNTL run) and experiment (AMSU-A run) run. Better values  
 462 are bolded. In parentheses, error statistics are shown over the mid-latitude region (30°S–60°S and 30°N–60°N) in the Northern and Southern  
 463 Hemisphere.

Trial Name	Bias				STDDEV			
	Global	NH	TR	SH	Global	NH	TR	SH
CNTL	-18.70	<b>-13.90</b> (-18.43)	-19.05	-27.45 (-19.84)	48.82	48.02 (26.71)	13.55	62.54 (38.55)
AMSU-A	<b>-18.59</b>	-17.39 ( <b>-16.95</b> )	<b>-17.73</b>	<b>-25.51</b> ( <b>-19.54</b> )	<b>42.42</b>	<b>31.55</b> ( <b>20.24</b> )	<b>12.41</b>	<b>58.29</b> ( <b>33.49</b> )

464  
 465 Even though the AMSU-A observations, including mperature information, are additionally assimilated in the  
 466 AMSU-A run, the AMSU-A run has a negative temperature bias that occurs in the CNTL run. It is related to the bias correction  
 467 applied to the AMSU-A observations in DART. As mentioned in section 4.3, the AMSU-A radiances are corrected by  
 468 eliminating the biases based on the departure between the observed radiances and the forward-simulated radiances from the  
 469 model background field. In addition, in this study, the bias correction coefficients were even updated at each cycle, using the  
 470 DART outputs from the last four cycles. Thus, the information on the model bias is included in the biases derived from the

471 correction scheme, which gradually fits the observations to the model background over the sequent assimilation cycles. As a  
472 result, the model bias still exists in the AMSU-A run as well as the CNTL run.

473 However, the global-mean STDDEV of 500 hPa geopotential height for the AMSU-A run is reduced to about 42 m  
474 as compared with the STDDEV (about 49 m) for the CNTL run, meaning that the 500 hPa geopotential height predictions are  
475 improved by assimilating the AMSU-A observations (Table 3). In particular, the error is largely reduced over the Northern  
476 Hemisphere. That is, the analysis impact is more significant in the Northern Hemisphere. It is inconsistent with the consensus  
477 that the assimilation impact of satellite observations is larger in the Southern Hemisphere, where the conventional data are  
478 sparse (Terasaki and Miyoshi, 2017; Yamazaki et al., 2023). As shown in Fig. 10a and b, a positive impact mainly occurs in  
479 the high-latitude region ( $> 60^{\circ}\text{N}$ ). In contrast, over the tropics and Southern Hemisphere, the error reduction is relatively  
480 smaller than over the Northern Hemisphere. In the tropics, the analysis error (about 14 m) is quite small for the CNTL run, as  
481 compared with the large errors of about 48 m and 63 m in the Northern Hemisphere and Southern Hemisphere, respectively.  
482 Following Judt (2020), it was demonstrated that the tropical atmosphere has longer predictability than the extratropical  
483 atmosphere. Thus, the AMSU-A observations are conservatively assimilated in the tropics due to the small forecast errors,  
484 leading to less analysis impact.

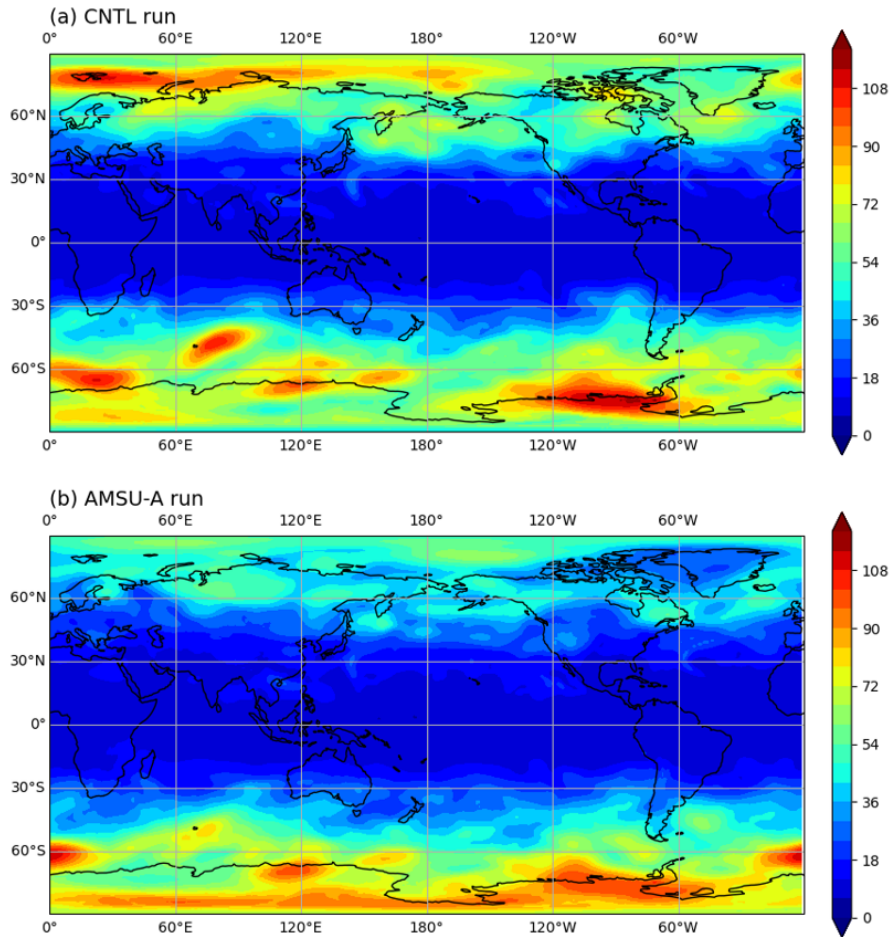


485 **Figure 9.** Mean bias of the first-guess departure for the radiosonde temperature measurements for the control (CNTL run: circle symbol and  
486 black line) and experiment (AMSU-A run: square symbol and red line) runs. Horizontal lines indicate 99% confidence intervals.  
487  
488

489 It is noted that the AMSU-A assimilation impact is neutral in the high-latitude region ( $> 60^{\circ}\text{S}$ ) over the Southern  
490 Hemisphere. In contrast, in the high-latitude region ( $> 60^{\circ}\text{N}$ ) over the Northern Hemisphere, the assimilation impact is  
491 significant. It is because the AMSU-A observations were not assimilated in the high latitude region ( $> 60^{\circ}\text{S}$ ) over the Southern  
492 Hemisphere during the Southern Hemisphere winter season when the trial runs were conducted (mentioned in section 4.1),  
493 resulting in the neutral analysis impact. Thus, if the high-latitude regions (i.e.,  $60^{\circ}\text{S}$ - $90^{\circ}\text{S}$  and  $60^{\circ}\text{N}$ - $90^{\circ}\text{N}$ ) are extracted in the  
494 error computation over both hemispheres, the analysis impact is still significant, but the difference in the analysis impact  
495 between both hemispheres considerably decreases (Table 3). It is still a challenging issue to assimilate the satellite radiances  
496 over the Antarctic continent, because of the complex topography, extreme weather condition, and large errors in the numerical



497 model. In particular, as the conventional observations are quite sparse in the high latitude region, the forecast errors are  
 498 relatively larger than the other latitudinal regions (i.e., the tropics and mid-latitude region, shown in Fig. 10a). In addition, the  
 499 trial period (11 August – 30 September 2014) is the Southern Hemisphere winter season when the Antarctic continent was  
 500 under extremely cold weather conditions. In fact, in the pre-trial run, we found that the analysis field was degraded near the  
 501 Antarctic continent by assimilating the AMSU-A observations. Thus, to prevent the analysis degradation, the AMSU-A  
 502 observations were rejected over the high latitude region ( $> 60^{\circ}\text{S}$ ) in the Southern Hemisphere. The assimilation of the AMSU-  
 503 A observation in the Antarctic region will be handled in future work.  
 504



505 **Figure 10.** Spatial distribution of the standard deviation (STDDEV) of ~~the analysis of the~~ 500 hPa geopotential height for the (a) control run  
 506 (CNTL) and (b) experiment (AMSU-A) runs, derived against the ERA5 reanalysis.  
 507  
 508

509 Figure 11 shows the normalized difference of STDDEV of temperature, zonal wind, and meridional wind between  
 510 the AMSU-A run and CNTL run, depending on the latitudinal regions (i.e., global, Northern/Southern Hemispheres, and  
 511 tropics). The STDDEV difference is normalized by the STDDEV for the CNTL run. A negative value means that assimilating  
 512 the AMSU-A observations provide analysis benefit. In contrast, a positive value indicates that the analysis error increases for  
 513 the AMSU-A run compared with the error for the CNTL run, implying a negative analysis impact of the AMSU-A observations.

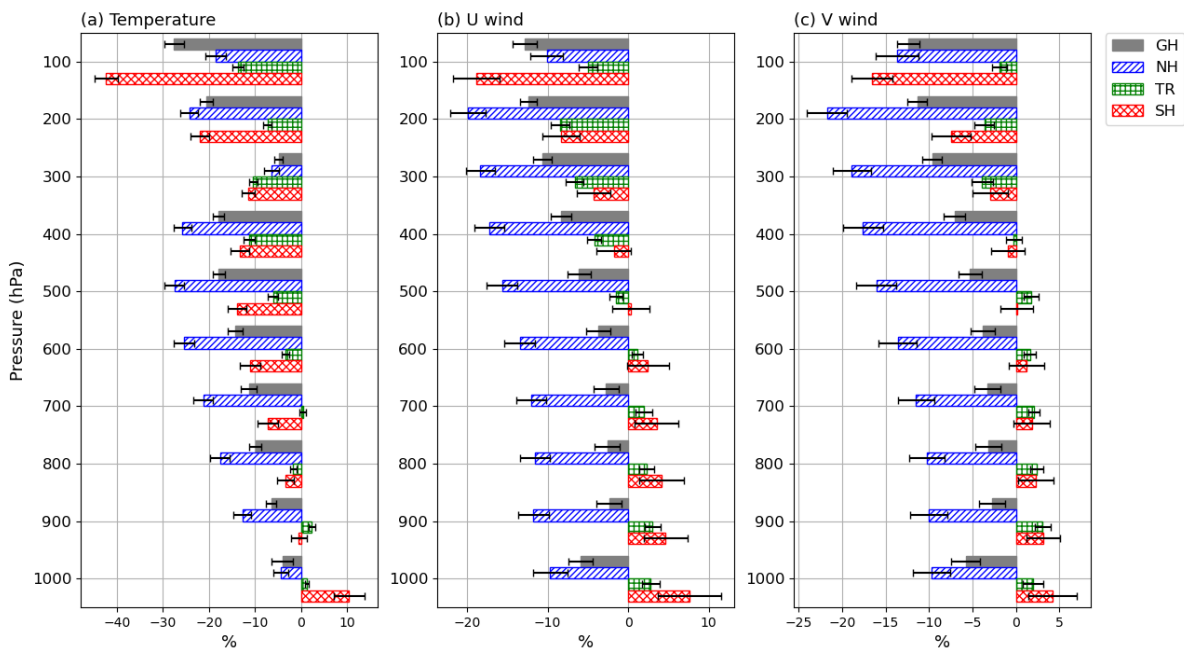
514 For the temperature, the global-mean analysis errors are significantly reduced in the whole troposphere and lower  
 515 stratosphere for the AMSU-A run, as compared with the CNTL run. Large error reduction occurs in the lower stratosphere (-  
 516 28% and -21% in 100 hPa and 200 hPa, respectively), which is consistent with the large gap between the STDDEVs of the  
 517 first-guess departure and the analysis departure for the stratospheric AMSU-A channels (channels 9–11) whose peak of the  
 518 weighting function is above 200 hPa (shown in Fig. 7). Similar to the results of the 500 hPa geopotential height, a strong error  
 519 reduction mainly occurs in the Northern Hemisphere where the error reduces up to about 28% in the 500 hPa pressure level

520 (Fig. 11a). The error decrease trends are consistent with the trends of the first-guess departure errors of the radiosonde  
 521 temperature measurements in which a significant error decrease occurs in the 500 hPa layer (Fig. 6a). However, in the lower  
 522 stratosphere (100 hPa pressure level), the analysis error decreases up to about 45% in the Southern Hemisphere.

523 For two wind components (i.e., zonal and meridional winds), similar to the results of the temperature, the global-  
 524 mean analysis errors for the AMSU-A run overall decrease in the whole troposphere and lower stratosphere (Fig. 11b and c).  
 525 It is noted that the magnitude of the error decrease tends to increase with height, reaching about -13% in the 100 hPa for the  
 526 zonal and meridional wind. Moreover, most analysis impact is made in the Northern Hemisphere, except in the 100 hPa where  
 527 the maximum error decrease occurs in the Southern Hemisphere. However, over the Southern Hemisphere, the analysis errors  
 528 for the AMSU-A runs are larger than the errors for the CNTL run in the middle and lower troposphere. For the spatial pattern  
 529 of the STDDEV of two wind components (not shown), it is found that the error increment mainly occurs in the high latitude  
 530 region ( $> 60^{\circ}\text{S}$ ) where the AMSU-A data were not assimilated for the AMSU-A run. Considering that the temperature fields  
 531 above the latitude of  $60^{\circ}\text{S}$  were only updated by the AMSU-A assimilation, the analysis degradation is possibly due to the  
 532 discontinuity of the latitudinal temperature gradient near the latitude of  $60^{\circ}\text{S}$ .

533 In the model humidity field, a positive analysis impact only occurs in the Northern Hemisphere (not shown), but is  
 534 not as significant as the abovementioned parameters (i.e., 500 hPa geopotential height, temperature, and winds). As a further  
 535 study, we plan to assimilate the Microwave Humidity Sounder (MHS) providing information on the vertical structure of  
 536 humidity so that the initial condition of model humidity is improved.

537



538

539 **Figure 11.** Normalized difference of the standard deviation (STDDEV) of the analysis of (a) temperature, (b) zonal wind, and (c) meridional  
 540 wind between the experiment (AMSU-A) run and the control (CNTL) run, derived against the ERA5 reanalysis. Hatched colors indicate the  
 541 latitude regions (global: grey, Northern Hemisphere: blue, tropics: green, and Southern Hemisphere: red). Horizontal lines indicate 99%  
 542 confidence intervals.

## 543 8 Summary

544 In this study, we attempted to assimilate the AMSU-A observations using the global data assimilation system  
 545 consisting of DART and CESM. To make the AMSU-A data available to be assimilated, preprocessing steps were developed,  
 546 which include quality control (i.e., outlier test and channel selection), spatial thinning, and bias correction (i.e., scan-bias  
 547 correction and air-mass-bias correction). In addition, the observation error covariance matrix was estimated, but only its  
 548 diagonal components were employed in DART because the inter-channel error correlation is not considered in the current

549 version of DART. To counteract the inter-channel error correlation, the diagonal components were inflated.

550 To assess the impact of the AMSU-A observations on the DART-derived analysis, trial experiments were conducted  
551 from 11 August to 30 September 2014. The derived analysis fields were verified using the ERA5 as the reference. For the  
552 primary atmospheric parameters (i.e., 500 hPa geopotential height, temperature, zonal wind, and meridional wind), an  
553 additional analysis benefit is provided by assimilating the AMSU-A observations on top of the DART data assimilation system  
554 which already makes use of the conventional ground-based observations. In particular, a large analysis impact is shown in the  
555 Northern Hemisphere where the analysis errors of the temperature and two wind components are significantly reduced in the  
556 whole troposphere. However, in the tropics, the analysis impact is relatively small due to the small forecast errors. Compared  
557 with the Northern Hemisphere, less analysis impact in the Southern Hemisphere seems to be due to the reduction in the number  
558 of assimilated AMSU-A observations. The AMSU-A observations are rejected in the high latitude regions ( $> 60^{\circ}\text{S}$ ) during the  
559 Southern Hemisphere winter season, because assimilating these observations worsens the analysis quality.

560

#### 561 **Code and data availability.**

562 DART version 9.11.13 was obtained from <https://github.com/NCAR/DART>. CESM version 2.1.0 is released at  
563 <https://github.com/ESCOMP/CESM/tree/release-cesm2.1.0>. Atmospheric initial conditions and the baseline observations at  
564 the BUFR format were obtained from the NCAR RDA (<https://rda.ucar.edu/datasets/ds337.0> or <https://doi.org/10.5065/Z83F-N512>). AMSU-A Level-1B version 5 data from the Aqua satellite, including the calibrated brightness temperatures, were  
565 downloaded from the NASA Goddard Earth Sciences Data and Information Services Center  
566 (<https://www.earthdata.nasa.gov/eosdis/daacs/gesdisc>). In addition, AMSU-A Level-1B from NOAA-19, MetOp-A, and  
567 MetOp-B satellites were downloaded from the atmosphere product section in the EUMETSAT product navigator  
568 (<https://navigator.eumetsat.int>). The ECMWF ERA5 hourly data on pressure levels were acquired from the Copernicus Climate  
569 Change Service (C3S) Climate Data Store (<https://cds.climate.copernicus.eu/cdsapp#!/dataset/reanalysis-era5-pressure-levels>).  
570 As well as the software codes, the model outputs are available at <https://doi.org/10.5281/zenodo.7714755> and  
571 <https://doi.org/10.5281/zenodo.7983459>.

572

573  
574 **Author contributions.** YN and YC conceptualized the research idea. YN and YC developed the methods with assistance from  
575 HS and YK. YN led the writing of the manuscript with support from YC, HS, and KR. YC, HS, KR, and JK involved in writing  
576 the final version of the manuscript, whereas YK provided feedback on it.

577

578 **Competing interests.** The authors declare no conflicts of interest.

579

580 **Acknowledgements.** This project is sponsored by Korea Polar Research Institute (KOPRI) grant funded by the Ministry of  
581 Oceans and Fisheries (KOPRI PE23010). NCAR is supported by the U.S. National Science Foundation (NSF). Any opinions  
582 expressed here are not necessarily those of NCAR or the NSF. Hyo-Jong Song and Youngchae Kwon are supported by Korea  
583 Environment Industry & Technology Institute (KEITI) through “Climate Change R&D Project for New Climate Regime”,  
584 funded by Korea Ministry of Environment (MOE) (2022003560006).

585

- 587 Anderson, J. L.: An ensemble adjustment Kalman filter for data assimilation, *Mon. Weather Rev.*, 129, 2884-2903,  
588 doi:10.1175/1520-0493(2001)129<2884:AEAKFF>2.0.CO;2, 2001.
- 589 Anderson, J. L.: Localization and sampling error correction in ensemble Kalman filter data assimilation, *Mon. Weather Rev.*,  
590 140, 2359-2371, doi:10.1175/MWR-D-11-00013.1, 2012.
- 591 Anderson, J., Hoar, T., Raeder, K., Liu, H., Collins, N., Torn, R., and Avellano, A.: The data assimilation research testbed: A  
592 community facility, *B. Am. Meteorol. Soc.*, 90, 1283-1296, doi:10.1175/2009BAMS2618.1, 2009.
- 593 Bormann, N., and Bauer, P.: Estimates of spatial and interchannel observation-error characteristics for current sounder  
594 radiances for numerical weather prediction. I: Methods and application to ATOVS data, *Q. J. Roy. Meteor. Soc.*, 136, 1036-  
595 1050, doi:10.1002/qj.616, 2010.
- 596 Campbell, W. F., Satterfield, E. A., Ruston, B., and Baker, N. L.: Accounting for correlated observation error in a dual-  
597 formulation 4D variational data assimilation system, *Mon. Weather Rev.*, 145, 1019-1032, doi:10.1175/MWR-D-16-0240.1,  
598 2017.
- 599 Coniglio, M. C., Romine, G. S., Turner, D. D., and Torn, R. D.: Impacts of targeted AERI and Doppler lidar wind retrievals on  
600 short-term forecasts of the initiation and early evolution of thunderstorms, *Mon. Weather Rev.*, 147, 1149-1170., doi:  
601 10.1175/MWR-D-18-0351.1, 2019.
- 602 Danabasoglu, G., Lamarque, J. F., Bacmeister, J., Bailey, D. A., DuVivier, A. K., Edwards, J., et al.: The community earth  
603 system model version 2 (CESM2), *J. Adv. Model. Earth Sy.*, 12, 1-35, doi:10.1029/2019MS001916, 2020.
- 604 Desroziers, G., Berre, L., Chapnik, B., and Poli, P.: Diagnosis of observation, background and analysis-error statistics in  
605 observation space, *Q. J. Roy. Meteor. Soc.*, 131, 3385-3396, doi:10.1256/qj.05.108, 2005.
- 606 Duncan, D. I., Bormann, N., Geer, A. J., and Weston, P.: Assimilation of AMSU-A in All-Sky Conditions, *Mon. Weather Rev.*,  
607 150, 1023-1041, doi:10.1175/MWR-D-21-0273.1, 2022.
- 608 English, S., McNally, T., Bormann, N., Salonen, K., Matricardi, M., Horanyi, A., Rennie, M., Janisková, M., Michele, S. D.,  
609 Geer, A., Tomaso E. D., Cardinali, C., Rosnay, P., Sabater, J. M., Bonavita, M., Albergel, C., Engelen, R., Thépaut, J.: Impact  
610 of Satellite Data, ECMWF Technical Memorandum, 711, ECMWF Reading, UK, 2013.
- 611 Eresmaa, R., Letertre-Danczak, J., Lupu, C., Bormann, N., and McNally, A. P.: The assimilation of Cross-track Infrared  
612 Sounder radiances at ECMWF, *Q. J. Roy. Meteor. Soc.*, 143, 3177-3188, doi:10.1002/qj.3171, 2017.
- 613 Eyre, J. R., Bell, W., Cotton, J., English, S. J., Forsythe, M., Healy, S. B., and Pavelin, E. G.: Assimilation of satellite data in  
614 numerical weather prediction. Part II: Recent years, *Q. J. Roy. Meteor. Soc.*, 148, 521-556, doi:10.1002/qj.4228, 2022.
- 615 Eyre, J. R., English, S. J., and Forsythe, M.: Assimilation of satellite data in numerical weather prediction. Part I: The early  
616 years, *Q. J. Roy. Meteor. Soc.*, 146, 49-68, doi:10.1002/qj.3654, 2020.
- 617 El Gharamti, M., Raeder, K., Anderson, J., and Wang, X.: Comparing adaptive prior and posterior inflation for ensemble filters  
618 using an atmospheric general circulation model, *Mon. Weather Rev.*, 147, 2535-2553, doi:10.1175/MWR-D-18-0389.1, 2019.
- 619 Goldberg, M. D., Crosby, D. S., and Zhou, L.: The limb adjustment of AMSU-A observations: Methodology and validation, *J.*  
620 *Appl. Meteorol. Clim.*, 40, 70-83, doi:10.1175/1520-0450(2001)040<0070:TLAOAA>2.0.CO;2, 2001.
- 621 Grody, N., Weng, F., and Ferraro, R.: Application of AMSU for obtaining water vapor, cloud liquid water, precipitation, snow  
622 cover, and sea ice concentration, 10th International TOVS Study Conference, International TOVS Working Group (ITWG),  
623 1999.
- 624 Grody, N., Zhao, J., Ferraro, R., Weng, F., and Boers, R.: Determination of precipitable water and cloud liquid water over  
625 oceans from the NOAA 15 advanced microwave sounding unit, *J. Geophys. Res.*, 106, 2943-2953, doi:  
626 10.1029/2000JD900616, 2001.
- 627 Harris, B. A. and Kelly, G.: A satellite radiance-bias correction scheme for data assimilation, *Q. J. Roy. Meteor. Soc.*, 127,

628 1453-1468, doi:10.1002/qj.49712757418, 2001.

629 Hoar, T. J., Raeder, K., Anderson, J. L., Steward, J., El Gharamti, M., Johnson, B. K., Romine, G., Ha, S., and Mizzi, A. P.:  
630 DART: Empowering Geoscience with Improved Ensemble Data Assimilation, 2020 AGU Fall Meeting, American Geophysical  
631 Union, 2020.

632 Hurrell, J. W., Holland, M. M., Gent, P. R., Ghan, S., Kay, J. E., Kushner, P.J., et al.: The community earth system model: a  
633 framework for collaborative research, *B. Am. Meteorol. Soc.*, 94, 1339-1360, doi:10.1175/BAMS-D-12-00121.1, 2013.

634 Joo, S., Eyre, J., and Marriott, R.: The impact of MetOp and other satellite data within the Met Office global NWP system  
635 using an adjoint-based sensitivity method, *Mon. Weather Rev.*, 141, 3331-3342, doi:10.1175/MWR-D-12-00232.1, 2013.

636 Judt, F.: Atmospheric predictability of the tropics, middle latitudes, and polar regions explored through global storm-resolving  
637 simulations, *J. Atmos. Sci.*, 77, 257–276, doi:10.1175/JAS-D-19-0116.1, 2020.

638 Kalnay, E.: *Atmospheric Modeling, Data Assimilation and Predictability*. Cambridge University Press, 2003.

639 Kay, J. E., Deser, C., Phillips, A., Mai, A., Hannay, C., Strand, G., et al.: The Community Earth System Model (CESM) large  
640 ensemble project: A community resource for studying climate change in the presence of internal climate variability, *B. Am.*  
641 *Meteorol. Soc.*, 96, 1333-1349, doi:10.1175/BAMS-D-13-00255.1, 2015.

642 Kim, S. M. and Kim, H. M.: Forecast sensitivity observation impact in the 4DVAR and hybrid-4DVAR data assimilation  
643 systems, *J. Atmos. Ocean. Tech.*, 36, 1563-1575, doi:10.1175/JTECH-D-18-0240.1, 2019.

644 Liu, H., Anderson, J., and Kuo, Y. H.: Improved analyses and forecasts of Hurricane Ernesto's genesis using radio occultation  
645 data in an ensemble filter assimilation system, *Mon. Weather Rev.*, 140, 151-166, doi:10.1175/MWR-D-11-00024.1, 2012.

646 Menzel, W. P., Schmit, T. J., Zhang, P., and Li, J.: Satellite-based atmospheric infrared sounder development and applications,  
647 *B. Am. Meteorol. Soc.*, 99, 583-603, doi:10.1175/BAMS-D-16-0293.1, 2018.

648 Migliorini, S. and Candy, B.: All-sky satellite data assimilation of microwave temperature sounding channels at the Met Office,  
649 *Q. J. Roy. Meteor. Soc.*, 145, 867–883, doi:10.1002/qj.3470, 2019.

650 Migliorini, S., Piccolo, C., and Rodgers, C. D.: Use of the information content in satellite measurements for an efficient  
651 interface to data assimilation, *Mon. Weather Rev.*, 136, 2633-2650, doi:10.1175/2007MWR2236.1, 2008.

652 Mo, T.: AMSU-A antenna pattern corrections, *IEEE Trans. Geosci. Remote Sens.*, 37, 103-112, doi: 10.1109/36.739131, 1999.

653 Ochotta, T., Gebhardt, C., Saupe, D., and Wergen, W.: Adaptive thinning of atmospheric observations in data assimilation with  
654 vector quantization and filtering methods, *Q. J. Roy. Meteor. Soc.*, 131, 3427-3437, doi:10.1256/qj.05.94, 2005.

655 Raeder, K., Anderson, J. L., Collins, N., Hoar, T. J., Kay, J. E., Lauritzen, P. H., and Pincus, R.: DART/CAM: An ensemble  
656 data assimilation system for CESM atmospheric models, *J. Clim.*, 25, 6304-6317, doi:10.1175/JCLI-D-11-00395.1, 2012.

657 Raeder, K., Hoar, T. J., El Gharamti, M., Johnson, B. K., Collins, N., Anderson, J. L., Steward, J., and Coady, M.: A new  
658 CAM6+ DART reanalysis with surface forcing from CAM6 to other CESM models, *Sci. Rep.*, 11, 1-24, doi: 10.1038/s41598-  
659 021-92927-0, 2021.

660 Scheck, L., Weissmann, M., and Bernhard, M.: Efficient Methods to Account for Cloud-Top Inclination and Cloud Overlap in  
661 Synthetic Visible Satellite Images, *J. Atmos. Ocean. Tech.*, 35, 665-685, doi:10.1175/JTECH-D-17-0057.1, 2018.

662 Saunders, R., Hocking, J., Turner, E., Rayer, P., Rundle, D., Brunel, P., Vidot, J., Roquet, P., Matricardi, M., Gear, A., Bormann,  
663 N., and Lupu, C.: An update on the RTTOV fast radiative transfer model (currently at version 12), *Geosci. Model Dev.*, 11,  
664 2717-2737, doi:10.5194/gmd-11-2717-2018, 2018.

665 Stewart, L. M., Dance, S. L., Nichols, N. K., Eyre, J. R., and Cameron, J.: Estimating interchannel observation-error  
666 correlations for IASI radiance data in the Met Office system, *Q. J. Roy. Meteor. Soc.*, 140, 1236-1244, doi:10.1002/qj.2211,  
667 2014.

668 Terasaki, K. and Miyoshi, T.: Assimilating AMSU-A Radiances with the NICAM-LETKF, *J. Meteorol. Soc. Jpn.*, 95, 433–446,  
669 doi:10.2151/jmsj.2017-028, 2017.

670 Weston, P. P., Bell, W., and Eyre, J. R.: Accounting for correlated error in the assimilation of high-resolution sounder data, *Q.*

671 J. Roy. Meteor. Soc., 140, 2420–2429, doi:10.1002/qj.2306, 2014.

672 Yamazaki, A., Terasaki, K., Miyoshi, T., and Noguchi, S.: Estimation of AMSU-A radiance observation impacts in an LETKF-  
673 based atmospheric global data assimilation system: Comparison with EFSO and observing system experiments, *Weather*  
674 *Forecast.*, 38, 953–970, doi:10.1175/WAF-D-22-0159.1, 2023.

675 Zhang, M., Zupanski, M., Kim, M.-J., and Knaff, J. A.: Assimilating AMSU-A Radiances in the TC Core Area with NOAA  
676 Operational HWRF (2011) and a Hybrid Data Assimilation System: Danielle (2010), *Mon. Weather Rev.*, 141, 3889–2907,  
677 doi:10.1175/MWR-D-12-00340.1, 2013.

678 Zhou, Y., Liu, Y., Huo, Z., and Li, Y.: A preliminary evaluation of FY-4A visible radiance data assimilation by the WRF (ARW  
679 v4. 1.1)/DART (Manhattan release v9. 8.0)-RTTOV (v12. 3) system for a tropical storm case, *Geosci. Model Dev.*, 15, 7397-  
680 7420, doi:10.5194/gmd-15-7397-2022, 2022.

681 Zhu, Y., Liu, E., Mahajan, R., Thomas, C., Groff, D., Delst, P. V., Collard, A., Kleist, D., Treadon, R., and Derber, J. C.: All-  
682 Sky Microwave Radiance Assimilation in NCEP's GSI Analysis System, *Mon. Weather Rev.*, 144, 4709–4735,  
683 doi:10.1175/mwr-d-15-0445.1, 2016.

684